Robotica (2016) volume 34, pp. 2186–2204. © Cambridge University Press 2014
doi:10.1017/S0263574714002835

Design, kinematic and dynamic modeling of a novel tripod based manipulator

Dan Zhang* and Bin Wei

University of Ontario Institute of Technology, 2000 Simcoe Street North, Oshawa, Ontario, L1H 7K4, Canada

(Accepted November 26, 2014. First published online: December 23, 2014)

SUMMARY

This paper proposes a novel three-degrees-of-freedom (3-DOF) hybrid manipulator, 3PU*S-PU, which evolves from the general function (Gf) set theory. After discussing the advantages of this new type of hybrid manipulator, this report analyzes the kinematic and Jacobian matrix of the manipulator. Subsequently, the kinematic performances, including stiffness/compliance, and workspace, undergo analysis, followed by the multi-objective optimization of the compliance and workspace. The Lagrangian method provides the framework for briefly analyzing the dynamics of the proposed manipulator. Finally, the results of this assessment comprise a guideline for controlling the manipulator.

KEYWORDS: Gf set; Type synthesis; Tripod; Compliance; Multi-objective optimization; Hybrid manipulator.

1. Introduction

Constituting a major subject of scholarly research, the type synthesis of parallel manipulators represents a vital task for future developments, analysis, and applications of these devices. Type synthesis involves the use of various methods to combine the advantages of serial and parallel manipulators for the purposes of designing new application-orientated mechanisms. When designing a new type of parallel manipulator, creators need to expand beyond the conventional joints, such as the prismatic joint, revolute joint, universal joint, and spherical joint. Accordingly, they can use the parallelogram joint (Pa joint) or the pure-translational universal joint, the U* joint, which is also considered a special parallelogram. In addition, the double parallelogram joint (Pa2 joint) can represent a leg or part of a structure instead of a conventional fixed length leg or actuated leg, as the parallelogram structure possesses higher stiffness in comparison to the conventional legs. The parallelogram contains two links acting in parallel, which enables the legs to distribute the loads; in comparison, the normal leg contains only a single leg, so the stiffness factor can be improved for the parallelogram structure-based parallel robotics. In addition, by using a parallelogram, the tilting angle or rotation capacity can be improved.[1] Engineers have proposed numerous methods to provide guidance for designing new types of parallel manipulators and enhancing their performance. The most common approach for designing a new parallel manipulator is based on the Chebychev–Grübler–Kutzbach formula, from which several possibilities can be enumerated; however, this process involves cumbersome work. In ref. [2], the systematic enumeration method is suggested; this approach emanates from the idea that some functional requirements of the desired mechanisms can undergo transformation into structural characteristics. In ref. [3], the theory of groups of displacements forms the foundation for developing new architecture for four-degrees-of-freedom (3T1R) fully parallel manipulators by employing the parallelograms. This framework, which treats each parallelogram-based structure as a motion generator, suggests that the combination of different motion generators can create new types of parallel manipulators. Similarly, in ref. [4], two identical kinematic chains that serve as Schonflies-motion generators are proposed for the parallel manipulator,

* Corresponding author. E-mail: Dan.Zhang@uoit.ca

https://doi.org/10.1017/S0263574714002835 Published online by Cambridge University Press

which also employs parallelograms. Recently, the Gf set theory was proposed for the type synthesis of parallel manipulators.[5] Accordingly, this paper utilizes the Gf set framework for the development of its new proposed manipulator.

The organization of this paper is as follows: first, this research proposes a novel 3-DOF hybrid manipulator 3PU*S-PU, mainly evolved from the Gf set theory. Subsequently, Section 2 discusses the advantages of this new type of manipulator. Section 3 analyzes the kinematic and Jacobian matrix of this manipulator, while Section 4 assesses and optimizes the kinematic performances, which include stiffness/compliance and workspace; Section 5 conducts the multi-objective optimization for the compliance and workspace. Finally, the Lagrangian method provides the basis for analyzing the dynamics of the proposed manipulator in Section 6, and Section 7 provides the conclusion.

2. Re-designing of the Mechanism

The Gf set theory[5] has two classes. The first class is represented by $G_F^I(\,T_a\;0\;0\,;\;R_\alpha\;R_\beta\;0\,)$, and the second class is shown by $G_F^{II}(\,R_\alpha\;R_\beta\;0\,;\;T_a\;0\;0\,)$.

When working with the first class, the first step involves determining the total number of links, the number of active links, the number of passive links, and the number of actuators on the ith active link. To find these quantities, the following formula must be used according to the characteristics of the end-effector (EE)[5]:

$$F_D - \sum_{i=1}^{n} q_i = 0$$

$$N = F_D - \sum_{i=1}^{n} (q_i - 1) + p$$

$$N = n + p$$

$$n \leq F_D$$

$$q_i \leq F_D (i = 1, 2, 3, \ldots, n),$$

where F_D represents the dimension of the EE characteristics of parallel topologies, N denotes the number of limbs, n is the number of actuated limbs, q_i represents the number of actuators of the ith actuated limb, and p is the number of passive limbs.

Secondly, according to the intersection algorithms,[5] one needs to obtain the composition types of the EE characteristics for the class $G_F^I(\,T_a\;0\;0\,;\;R_\alpha\;R_\beta\;0\,)$;

Thirdly, according to the composition types of the EE characteristics that were obtained in step two, one can find the required kinematic legs/limbs with the necessary EE characteristics; in other words, this step will determine all of the possible kinematic chains. Finally, one can synthesize the specific desired parallel manipulator by assembling the kinematic limbs.

The procedure for the second class $G_F^{II}(\,R_\alpha\;R_\beta\;0\,;\;T_a\;0\;0\,)$ is similar to that of the first class; however, in the second step, one needs to find the composition types of the EE characteristics the second class $G_F^{II}(\,R_\alpha\;R_\beta\;0\,;\;T_a\;0\;0\,)$ rather than the first class.

The previously described procedure will result in the creation of a new hybrid 3PU*S-PU manipulator, shown in Fig. 1. Although many 3-DOF parallel manipulators can be created from the Gf set theory, some of these manipulators lack effectiveness. For example, the 3PU*S-$(CR)_o$ and 3PU*S-$(RC)_o$ parallel manipulators possess a rotation axis perpendicular to the moving platform. Specifically, these manipulators have two rotations, one of which revolves about the Z-axis; however, this rotation contradicts the aims of the authors, who desired two rotations about the X and Y axes that were parallel to the moving platform. In ref. [6], the authors proposed a hybrid head mechanism, 4UPS-PU, to serve as the head section of a groundhog-like mine rescue robot. The unique feature of this mechanism involves a central passive P-U type limb, which was incorporated in the mechanism to constrain the entire structure as a 3-DOF manipulator with two rotations about the X and Y axes and one translation along the Z-axis. In ref. [7], the authors provide a comprehensive discussion of hybridization in the context of engineering. Inspired by the design in ref. [6], the manipulator's

https://doi.org/10.1017/S0263574714002835 Published online by Cambridge University Press

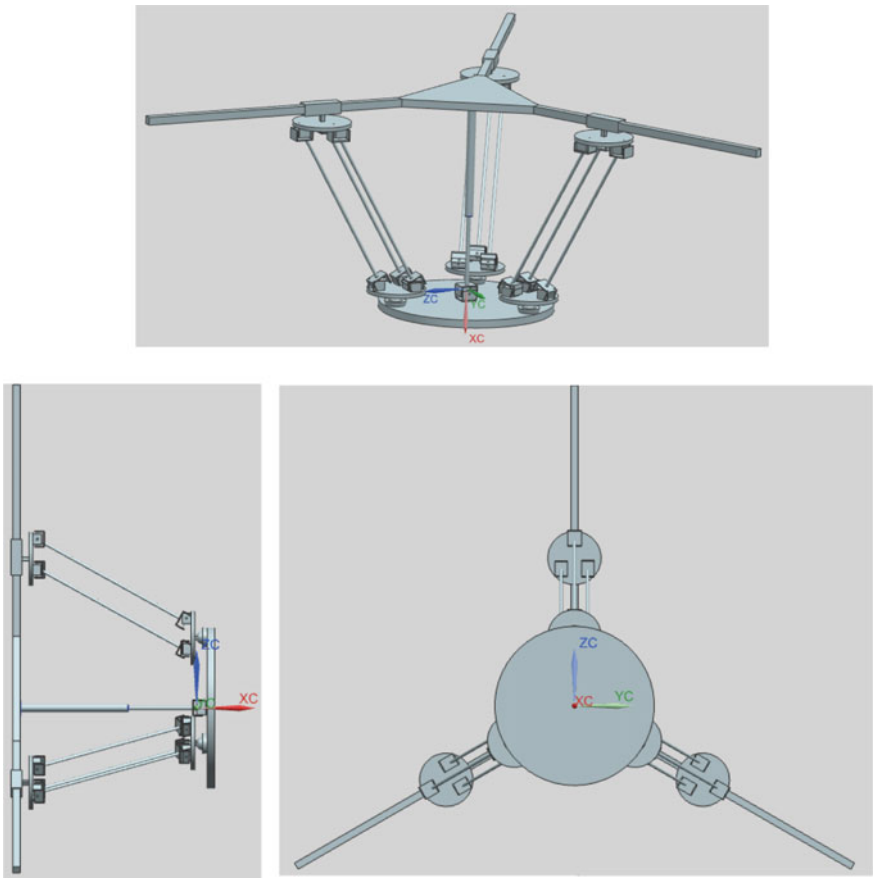


Fig. 1. Different views of 3PU*S-PU parallel manipulator.

passive middle leg is changed from the original to the P-U type; hence, the passive leg consists of a universal joint attached to the moving platform and a passive link fixed to the base. From this perspective, the manipulator contains three desired degrees of freedom, with two rotations about the *X* and *Y* axes and one translation along the *Z*-axis.

The newly proposed 3PU*S-PU manipulator involves several novel features. First, this device employs the U* joint, which significantly improves the stiffness of this parallel manipulator, as the pure-translational universal joint (U* joint) comprises part of the parallelogram family. As shown in Fig. 2, the structure of U* joint consists of two main parts: one section with two plates and another part with three links, which connect the two plates through universal joints. These joints enable the loads on the plate to be distributed by three links; hence, the use of the U* joint achieves greater stiffness than manipulators with only the normal leg. Not only does the U* joint increase the stiffness of the parallel manipulator but it also enhances the tilting angle or rotation capacity of the EE. Because the performance of the U* joint resembles that of the parallelogram, the parallelogram can increase the rotation capacity of the parallel manipulator.[1,8] Secondly, by changing the structure of the middle passive leg, especially its degrees of freedom, the entire parallel manipulator can undergo reconfiguration. For example, the removal of the middle passive leg causes the 3-DOF mechanism to become a device with six degrees of freedom.

This figure shows that the proposed manipulator only has 3-DOF, indicating the second purpose of the U* joint, which involves deactivation by the middle passive UP leg. Generally, machine tool design requires only 3-DOF: one translation along the *Z*-axis and two rotations about the *X* and *Y* axes. In order to obtain additional degrees of freedom in mechanisms based on the proposed hybrid manipulator, the middle passive leg can be removed, enabling the whole structure to become a six-degrees-of-freedom manipulator. Therefore, by changing the structure of the middle passive leg, the entire parallel manipulator can be reconfigured.

https://doi.org/10.1017/S0263574714002835 Published online by Cambridge University Press

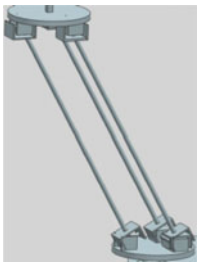


Fig. 2. Pure-translational universal joint.

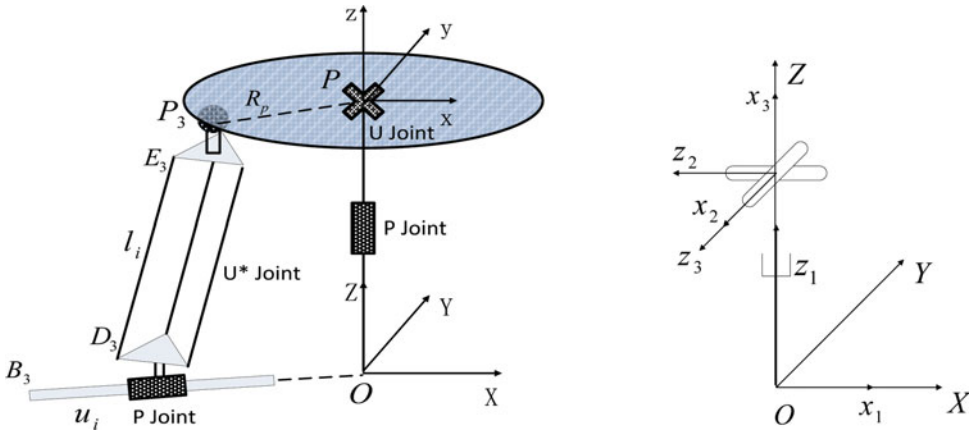


Fig. 3. Kinematic structures of 3PU*S-PU mechanism and central passive leg.

3. Kinematic Analysis of the Mechanism

3.1. Inverse kinematic of the mechanism

In the 3PU*S-PU mechanism shown in Fig. 3, the moving platform connects to the base by three active legs and one central passive leg. Each active leg contains the same architecture: P-U*-S. This U* joint connects to the base and moving platform by a prismatic joint and a spherical joint, respectively. In addition, the passive leg in the middle consists of a universal joint attached to the moving platform and a passive link fixed to the base. There are two purposes for using this passive leg; the first purpose involves constraining the moving platform to 3-DOF, while the second goal aims to further increase the stiffness of this parallel manipulator.[9] By actuating these three prismatic joints on the guide ways, the moving platform can achieve the desired motions.

The above figure shows that the joints attached to the base and moving platform are denoted by B_1, B_2, B_3 and P_1, P_2, P_3, respectively. For the purpose of analysis, the fixed coordinate system $O(X, Y, Z)$ is attached to the center of the base, which coincides with the fixed point of the passive leg. The X-axis points to the right and the Z-axis is perpendicular to the base, pointing upwards. In contrast, the moving coordinate system $P(x, y, z)$ is attached to the center of the moving platform, where the x-axis is parallel to the X-axis and the z-axis is perpendicular to the moving platform. The guide ways intersect at point O of the fixed coordinate system. While $angle1$ is the angle between the X-axis and the line OB_1, $angle2$ is the angle between the x-axis and the line PP_1. Finally, the radii of the base and the moving platform are denoted by R_b andR_p, respectively.

$$\alpha_1 = angle1, \quad \alpha_2 = angle1 + 120^\circ, \quad \alpha_3 = angle1 + 240^\circ, \quad \theta_1 = angle2,$$
$$\theta_2 = angle2 + 120^\circ, \quad \theta_3 = angle2 + 240^\circ,$$

where α_i $(i = 1, 2, 3)$ is the angle between the X-axis and line OB_i while θ_i indicates the angle between the x-axis and the line PP_i. With the fixed coordinate system, the coordinates of points B_1, B_2, and B_3 are denoted as ${}^oB_i (i = 1, 2, 3)$. While the coordinates of points P_1, P_2, and P_3 with respect to the moving coordinate system are denoted as ${}^PP_i$, the coordinates of points P_1, P_2, and

https://doi.org/10.1017/S0263574714002835 Published online by Cambridge University Press

P_3 with respect to the fixed coordinate system are denoted as ${}^{o}P_i$. In this case, ${}^{o}P_i$ can be written as follows:

$$ {}^{o}P_i = R_e{}^{P}P_i + {}^{o}P, \tag{1} $$

where ${}^{o}P = [\,0\ 0\ z_e\,]^T$ represents the coordinate of the center of the moving platform with respect to the fixed coordinate frame. R_e denotes the rotation matrix of the moving platform with respect to the base, and $\theta_x, \theta_y, \theta_z$ are the rotation angles of the moving platform with respect to the X, Y, and Z axes of the fixed coordinate system. And

$$ {}^{o}P_i = \begin{bmatrix} x_{pi}^{o} \\ y_{pi}^{o} \\ z_{pi}^{o} \end{bmatrix} = R_e{}^{P}P_i + {}^{o}P = \begin{bmatrix} -R_p\cos\theta_i\sin\theta_y \\ R_p\sin\theta_i\sin\theta_x - R_p\cos\theta_i\cos\theta_x\cos\theta_y \\ z_e + R_p\cos\theta_x\sin\theta_i + R_p\cos\theta_i\cos\theta_y\sin\theta_x \end{bmatrix}. \tag{2} $$

After differentiating the above equation, it yields

$$ \begin{bmatrix} \delta x_{pi}^{o} & \delta y_{pi}^{o} & \delta z_{pi}^{o} \end{bmatrix}^T = [J_i]\begin{bmatrix} \delta\theta_x & \delta\theta_y & \delta\theta_z & \delta x & \delta y & \delta z_e \end{bmatrix}^T, \tag{3} $$

and

$$ [J_i] = \begin{bmatrix} 0 & -R_p\cos\theta_i\cos\theta_y & 0 & 0 & 0 & 0 \\ R_p\sin\theta_i\cos\theta_x + R_p\cos\theta_i\sin\theta_x\cos\theta_y & R_p\cos\theta_i\cos\theta_x\sin\theta_y & 0 & 0 & 0 & 0 \\ -R_p\sin\theta_x\sin\theta_i + R_p\cos\theta_i\cos\theta_y\cos\theta_x & -R_p\cos\theta_i\sin\theta_y\sin\theta_x & 0 & 0 & 0 & 1 \end{bmatrix}. \tag{4} $$

From the vector loop equation, the following equation can be obtained:

$$ {}^{o}P_i - {}^{o}B_i - \mathrm{u}_i n_i = \mathrm{l}_i s_i, \tag{5} $$

where u_i is the actuated input. For example, the length of $B_i D_i$; n_i is the unit vector pointing along the rails, which can be written as $n_i = [\,-\cos\alpha_i\ -\sin\alpha_i\ 0\,]^T$; l_i is the length of the U* link constituting the length of fixed link $D_i E_i$ and s_i is the unit vector pointing along the link $D_i E_i$.

$$ \begin{aligned} \mathrm{l}_i s_i &= {}^{o}P_i - {}^{o}B_i - \mathrm{u}_i n_i \\ &= \begin{bmatrix} -R_p\cos\theta_i\sin\theta_y \\ R_p\sin\theta_i\sin\theta_x - R_p\cos\theta_i\cos\theta_x\cos\theta_y \\ z_e + R_p\cos\theta_x\sin\theta_i + R_p\cos\theta_i\cos\theta_y\sin\theta_x \end{bmatrix} - \begin{bmatrix} R_b\cos\alpha_i \\ R_b\sin\alpha_i \\ 0 \end{bmatrix} - \mathrm{u}_i\begin{bmatrix} -\cos\alpha_i \\ -\sin\alpha_i \\ 0 \end{bmatrix} \\ &= \begin{bmatrix} -R_p\cos\theta_i\sin\theta_y - R_b\cos\alpha_i + \mathrm{u}_i\cos\alpha_i \\ R_p\sin\theta_i\sin\theta_x - R_p\cos\theta_i\cos\theta_x\cos\theta_y - R_b\sin\alpha_i + \mathrm{u}_i\sin\alpha_i \\ z_e + R_p\cos\theta_x\sin\theta_i + R_p\cos\theta_i\cos\theta_y\sin\theta_x \end{bmatrix} = \begin{bmatrix} l_{ix} \\ l_{iy} \\ l_{iz} \end{bmatrix}. \end{aligned} \tag{6} $$

By dot multiplying Eq. (6) with itself, the following result is obtained:

$$ \mathrm{l}_i^2 = ({}^{o}P_i - {}^{o}B_i - \mathrm{u}_i n_i)^T({}^{o}P_i - {}^{o}B_i - \mathrm{u}_i n_i) = l_{ix}^2 + l_{iy}^2 + l_{iz}^2. \tag{7} $$

From Eq. (7), one can have the following:

$$ \mathrm{u}_i = \frac{-(2A\cos\alpha_i + 2B\sin\alpha_i) \pm \sqrt{(2A\cos\alpha_i + 2B\sin\alpha_i)^2 - 4(A^2 + B^2 + C^2 - \mathrm{l}_i^2)}}{2}, \tag{8} $$

where

$$ A = -R_p\cos\theta_i\sin\theta_y - R_b\cos\alpha_i, \quad B = R_p\sin\theta_i\sin\theta_x - R_p\cos\theta_i\cos\theta_x\cos\theta_y - R_b\sin\alpha_i, $$

https://doi.org/10.1017/S0263574714002835 Published online by Cambridge University Press

$$C = z_e + R_p \cos\theta_x \sin\theta_i + R_p \cos\theta_i \cos\theta_y \sin\theta_x.$$

This equation represents the completed inverse kinematic for the structure.

3.2. Jacobian of the mechanism

Since

$$\mathrm{l}_i^2 = \left(x_{pi}^o - R_b \cos\alpha_i + \mathrm{u}_i \cos\alpha_i\right)^2 + \left(y_{pi}^o - R_b \sin\alpha_i + \mathrm{u}_i \sin\alpha_i\right)^2 + \left(z_{pi}^o\right)^2, \tag{9}$$

the derivative of Eq. (9) with respect to x_{pi}^o, yields

$$\partial u_i(l_{ix}\cos\alpha_i + l_{iy}\sin\alpha_i) = -l_{ix}\partial x_{pi}^o. \tag{10}$$

Then, the derivative of Eq. (9) with respect to y_{pi}^o, yields

$$\partial u_i(l_{ix}\cos\alpha_i + l_{iy}\sin\alpha_i) = -l_{iy}\partial y_{pi}^o. \tag{11}$$

Finally, the derivative of Eq. (9) with respect to z_{pi}^o, yields

$$\partial u_i(l_{ix}\cos\alpha_i + l_{iy}\sin\alpha_i) = -z_{pi}^o \partial z_{pi}^o \quad \left(z_{pi}^o = l_{iz}\right). \tag{12}$$

Since $k_{ip} = l_{ix}\cos\alpha_i + l_{iy}\sin\alpha_i$, then the above three equations can be written as

$$\partial u_i = -\frac{l_{ix}}{k_{ip}}\partial x_{pi}^o, \quad \partial u_i = -\frac{l_{iy}}{k_{ip}}\partial y_{pi}^o, \quad \partial u_i = -\frac{l_{iz}}{k_{ip}}\partial z_{pi}^o. \tag{13}$$

From Eq. (13), one can obtain

$$3\partial u_i = -\frac{l_{ix}}{k_{ip}}\partial x_{pi}^o - \frac{l_{iy}}{k_{ip}}\partial y_{pi}^o - \frac{l_{iz}}{k_{ip}}\partial z_{pi}^o, \tag{14}$$

and

$$\partial u_i = \begin{bmatrix} \partial u_1 \\ \partial u_2 \\ \partial u_3 \end{bmatrix} = \frac{1}{3}\begin{bmatrix} -\frac{l_{ix}}{k_{ip}} & -\frac{l_{iy}}{k_{ip}} & -\frac{l_{iz}}{k_{ip}} \end{bmatrix} \cdot \begin{bmatrix} \partial x_{pi}^o \\ \partial y_{pi}^o \\ \partial z_{pi}^o \end{bmatrix} = \frac{1}{3}\begin{bmatrix} -\frac{l_{ix}}{k_{ip}} & -\frac{l_{iy}}{k_{ip}} & -\frac{l_{iz}}{k_{ip}} \end{bmatrix} \cdot [J_i] \begin{bmatrix} \delta\theta_x \\ \delta\theta_y \\ \delta\theta_z \\ \delta x \\ \delta y \\ \delta z_e \end{bmatrix}$$

$$= J_{\text{parallel}} \begin{bmatrix} \delta\theta_x \\ \delta\theta_y \\ \delta\theta_z \\ \delta x \\ \delta y \\ \delta z_e \end{bmatrix}, \tag{15}$$

https://doi.org/10.1017/S0263574714002835 Published online by Cambridge University Press

Table I. D–H parameters for the central passive leg.

i	a_i	d_i	α_i	θ_i
0	0	0	0	0
1	0	z_e	90°	−90°
2	0	0	90°	θ_x
3	0	0	−90°	θ_y

where

$$J_{\text{parallel}} = \frac{1}{3}\begin{bmatrix} \begin{bmatrix} -\frac{l_{1x}}{k_{1p}} & -\frac{l_{1y}}{k_{1p}} & -\frac{l_{1z}}{k_{1p}} \end{bmatrix}[J_1] \\ \begin{bmatrix} -\frac{l_{2x}}{k_{2p}} & -\frac{l_{2y}}{k_{2p}} & -\frac{l_{2z}}{k_{2p}} \end{bmatrix}[J_2] \\ \begin{bmatrix} -\frac{l_{3x}}{k_{3p}} & -\frac{l_{3y}}{k_{3p}} & -\frac{l_{3z}}{k_{3p}} \end{bmatrix}[J_3] \end{bmatrix}.$$

The twist of the moving platform is expressed as $t = [\,\delta\theta_x\ \delta\theta_y\ \delta\theta_z\ \ \delta x\ \delta y\ \ \delta z_e\,]^T$, and

$$\begin{bmatrix} \delta \mathrm{l}_1 \\ \delta \mathrm{l}_2 \\ \delta \mathrm{l}_3 \end{bmatrix} = \begin{bmatrix} \begin{bmatrix} \frac{l_{1x}}{\mathrm{l}_1} & \frac{l_{1y}}{\mathrm{l}_1} & \frac{l_{1z}}{\mathrm{l}_1} \end{bmatrix}[J_1] \\ \begin{bmatrix} \frac{l_{2x}}{\mathrm{l}_2} & \frac{l_{2y}}{\mathrm{l}_2} & \frac{l_{2z}}{\mathrm{l}_2} \end{bmatrix}[J_2] \\ \begin{bmatrix} \frac{l_{3x}}{\mathrm{l}_3} & \frac{l_{3y}}{\mathrm{l}_3} & \frac{l_{3z}}{\mathrm{l}_3} \end{bmatrix}[J_3] \end{bmatrix} \cdot \begin{bmatrix} \delta\theta_x \\ \delta\theta_y \\ \delta\theta_z \\ \delta x \\ \delta y \\ \delta z_e \end{bmatrix} = J_{co} \cdot \begin{bmatrix} \delta\theta_x \\ \delta\theta_y \\ \delta\theta_z \\ \delta x \\ \delta y \\ \delta z_e \end{bmatrix}. \tag{16}$$

The central passive leg, whose kinematic structure is shown in Fig. 3, can be viewed as a serial component. From Fig. 3, the D–H parameters of the passive leg are obtained in Table I.
And

$$Q_0 = \begin{bmatrix} 1 & 0 & 0 \\ 0 & 1 & 0 \\ 0 & 0 & 1 \end{bmatrix}, \quad Q_1 = \begin{bmatrix} 0 & 0 & -1 \\ -1 & 0 & 0 \\ 0 & 1 & 0 \end{bmatrix}, \quad Q_2 = \begin{bmatrix} \cos\theta_x & 0 & \sin\theta_x \\ \sin\theta_x & 0 & -\cos\theta_x \\ 0 & 1 & 0 \end{bmatrix},$$
$$Q_3 = \begin{bmatrix} \cos\theta_y & 0 & -\sin\theta_y \\ \sin\theta_y & 0 & \cos\theta_y \\ 0 & -1 & 0 \end{bmatrix}, \tag{17}$$

where Q_i comprises the rotation matrix from the ith frame to the $(i+1)$th frame of the passive leg. Given rotation matrix $R_e = Q_0 \cdot Q_1 \cdot Q_2 \cdot Q_3$, the following equations can be obtained through Eq. (17)[10]:

$$e_{41} = Q_0 e_{40}; \quad e_{42} = Q_0 Q_1 e_{40}; \quad e_{43} = Q_0 Q_1 Q_2 e_{40},$$

where e_{4i} is the third column of the rotation matrix $Q_0 Q_1 \cdots Q_{i-1}$ and $e_{40} = [\,0\ 0\ 1\,]^T$. The position vectors are expressed as follows:

$$r_{41} = Q_0 a_{41} + Q_0 Q_1 a_{42} + Q_0 Q_1 Q_2 a_{43}; \quad r_{42} = Q_0 Q_1 a_{42} + Q_0 Q_1 Q_2 a_{43}; \quad r_{43} = Q_0 Q_1 Q_2 a_{43},$$

where $a_{41} = [\,0\ 0\ z_e\,]^T$, $a_{42} = [\,0\ 0\ 0\,]^T$ and $a_{43} = [\,0\ 0\ 0\,]^T$. For the passive leg, the equation yields

$$J_{\text{serial}}\,\dot{\theta}_4 = t, \tag{18}$$

https://doi.org/10.1017/S0263574714002835 Published online by Cambridge University Press

where $\dot{\theta}_4 = [\dot{z}_e \ \dot{\theta}_x \ \dot{\theta}_y]$. The Jacobian matrix for the central passive leg of the mechanism J_{serial} can be expressed as follows:

$$J_{\text{serial}} = \begin{bmatrix} \text{zeros}(3,1) & e_{42} & e_{43} \\ e_{41} & e_{42} \times r_{42} & e_{43} \times r_{43} \end{bmatrix}. \tag{19}$$

The Jacobian matrix of the entire mechanism can be written as[6]

$$J = J_{\text{parallel}} J_{\text{serial}}. \tag{20}$$

4. Compliance Modeling, Global Condition Index, and Single-Objective Optimization

4.1. Kinetostatic modeling

The general derivation process for the Cartesian compliance matrix occurs in the following set of equations. The first equation is based on the principle of virtual work[10]:

$$(J_{\text{co}} J_{\text{serial}})^T \tau = {J_{\text{serial}}}^T w, \tag{21}$$

where τ represents the vector of actuator forces and w is the force or torque applied to the moving platform. An actuator compliance matrix, C, is defined as

$$C\tau = \Delta\rho, \tag{22}$$

where $\Delta\rho$ denotes the joint displacement. Equation (21) can be rewritten as follows:

$$\Delta\rho = C(J_{\text{co}} J_{\text{serial}})^{-T} {J_{\text{serial}}}^T w. \tag{23}$$

Furthermore, for a small displacement vector $\Delta\rho$, the equation yields

$$\Delta\rho = J_{co}\Delta c, \tag{24}$$

where Δc is a vector of small Cartesian displacement and rotation.[10] By inserting Eq. (24) into (23) and rearranging the equation, the following can be derived:

$$\Delta c = J_{\text{serial}}(J_{\text{co}} J_{\text{serial}})^{-1} C (J_{\text{co}} J_{\text{serial}})^{-T} {J_{\text{serial}}}^T w. \tag{25}$$

Consequently, the Cartesian compliance matrix is obtained as

$$C_c = J_{\text{serial}}(J_{\text{co}} J_{\text{serial}})^{-1} C (J_{\text{co}} J_{\text{serial}})^{-T} J_{\text{serial}}^T, \tag{26}$$

where C_c is a symmetrical positive semi-definite (6×6) matrix. In the above calculation, the compliance matrix is preferred over the stiffness matrix because matrix C_c cannot be inverted.[10]

4.2. Single-objective optimization

The objective function should be established in order to implement the optimization process. To minimize the compliance, a trace of the Cartesian compliance represents the objective function.

1. Objective function:

$$ObjF = \sum_{i=1}^{6} C_c(i,i).$$

https://doi.org/10.1017/S0263574714002835 Published online by Cambridge University Press

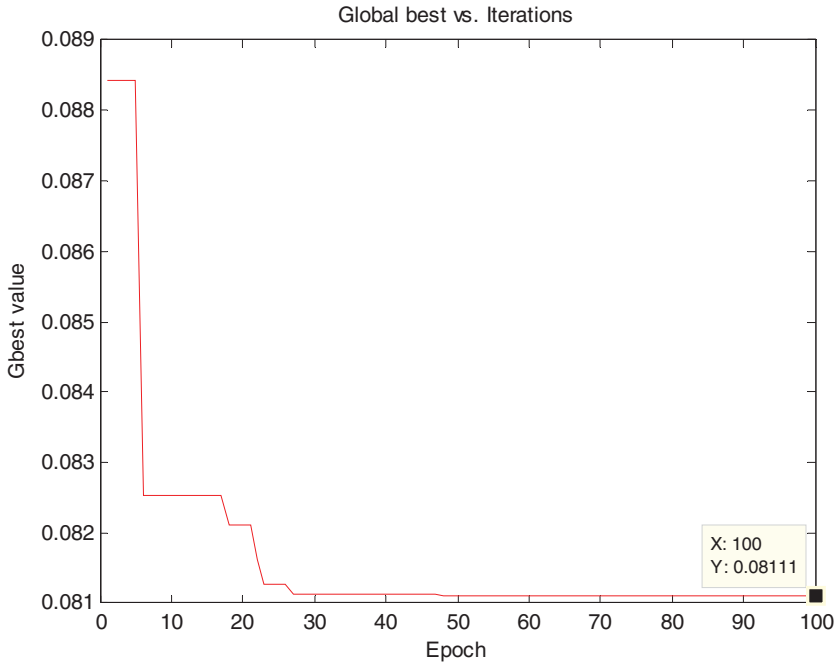


Fig. 4. Optimization result of global compliance using DE.

2. Design variables:

$$D = [R_P, R_b, L, angle1, angle2],$$

where L is the length of the fixed link on the U* joint, under the assumption that each U* joint is the same, so that $l_1 = l_2 = l_3 = L$.

3. Constraints:
For the purpose of analysis, this section assumes the following constraints:

$$R_P \in [0.04, 0.15]m, \quad R_b \in [0.4, 0.6]m, \quad l_i \in [0.35, 0.5]m, \quad angle1 \in [15^\circ, 45^\circ],$$
$$angle2 \in [15^\circ, 45^\circ].$$

Then, the optimization is performed under the following configuration:

$$\alpha_1 = angle1, \quad \alpha_2 = angle1 + 120^\circ, \quad \alpha_3 = angle1 + 240^\circ,$$
$$\theta_1 = angle2, \quad \theta_2 = angle2 + 120^\circ, \quad \theta_3 = angle2 + 240^\circ,$$
$$\theta_x = 90^\circ, \quad \theta_y = -90^\circ, \quad z_e = 0.3.$$

The results are obtained by using a differential evolution (DE) optimization algorithm with several parameters: a population size of 75; a maximum value for generations of 100; a crossover ratio of 1; and a constraint-dependent mutation function.

After approximately 50 generations, the optimal parameters are obtained as follows: $[R_P, R_b, L, angle1, angle2] = [0.15m, 0.5716m, 0.35m, 0.2740 \text{ rad}, 0.2995 \text{ rad}]$. As seen in Fig. 4, which displays the results of the global compliance optimization, the optimum value for the objective function is 0.08111. In order to obtain the minimum global compliance for the manipulator, the radius of the moving platform should be 0.15m, the radius of the base should be 0.57m, the length of the fixed link should be 0.35m, the angle between the X-axis and line OB_i should be 0.27 rad, and the

https://doi.org/10.1017/S0263574714002835 Published online by Cambridge University Press

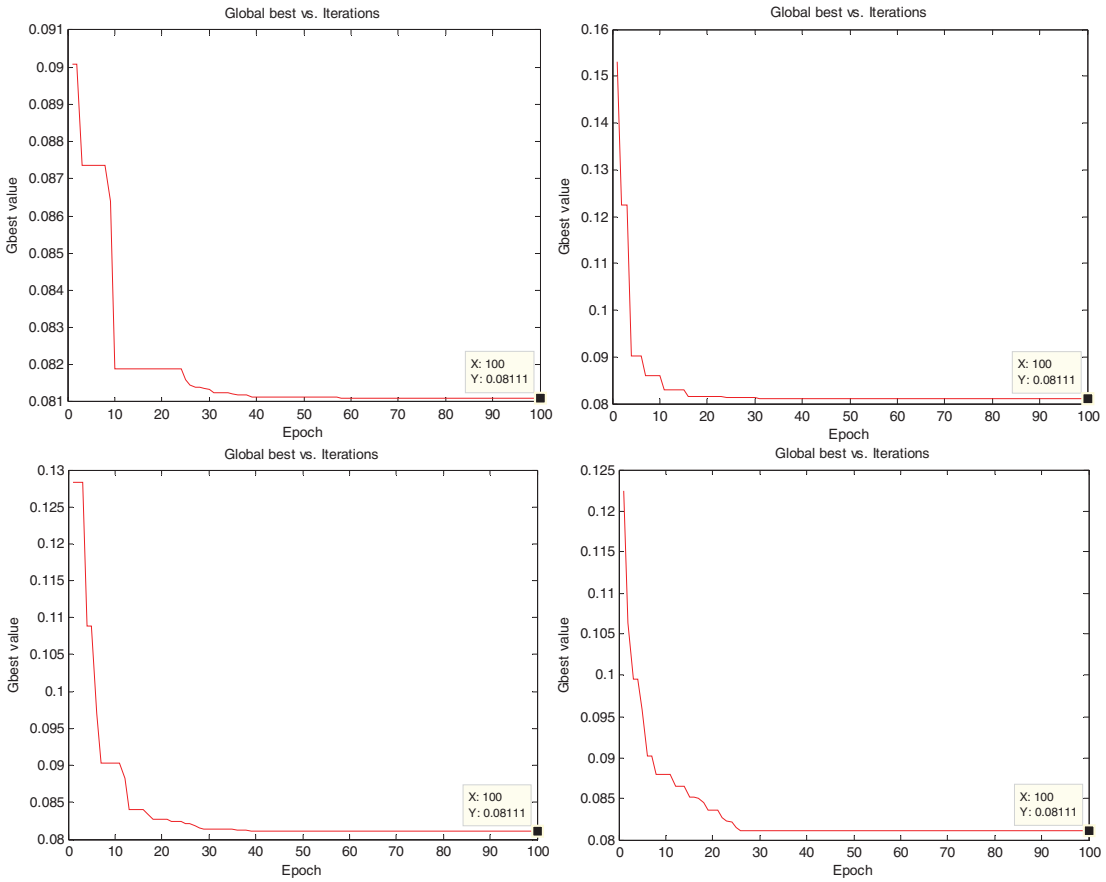


Fig. 5. Optimization results of global compliance using DE.

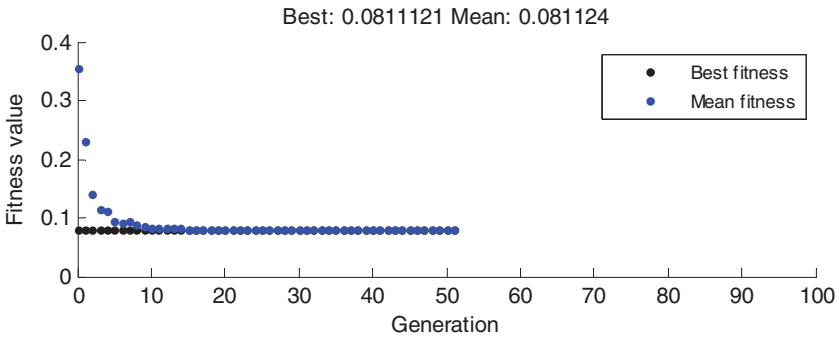


Fig. 6. Optimization result of global compliance using GA.

angle between the X-axis and line PP_i should be 0.29 rad. After running four trials of DE, the analysis obtained the same results, as shown in Fig. 5.

In addition, the use of genetic algorithms obtains the same results with the same tuning parameters.

Figure 6 displays a plot of the best function values in each generation versus the iteration number. The black points denote the best fitness values while the blue points denote the mean fitness values in each generation. After 51 generations, the optimal parameters are obtained as follows:

$$[R_P, R_b, L, angle1, angle2] = [0.15m, 0.57m, 0.35m, 0.27 \text{ rad}, 0.28 \text{ rad}].$$

https://doi.org/10.1017/S0263574714002835 Published online by Cambridge University Press

The optimum value for the objective function is 0.08. These results suggest that in order to obtain the minimum global compliance for the manipulator, the radius of the moving platform should be 0.15m, the radius of the base should be 0.57m, the length of the fixed link should be 0.35m, the angle between the X-axis and line OB_i should be 0.27 rad, and the angle between the X-axis and line PP_i should be 0.28 rad.

After performing optimization and selecting the optimized solutions, the compliance matrix is

$$C = \begin{bmatrix} 0.0403 & 0 & 0 & 0 & 0 & 0 \\ 0 & 0.0403 & 0 & 0 & 0 & 0 \\ 0 & 0 & 0 & 0 & 0 & 0 \\ 0 & 0 & 0 & 0 & 0 & 0 \\ 0 & 0 & 0 & 0 & 0 & 0 \\ 0 & 0 & 0 & 0 & 0 & 0.0005 \end{bmatrix}.$$

The compliance sum of this matrix is 0.0811.

Before optimization, $R_P = 0.1$, $R_b = 0.3$, $L = 0.4$, $angle1 = 30^\circ$, $angle2 = 30^\circ$, the compliance matrix is

$$C = \begin{bmatrix} 0.1185 & 0 & 0 & 0 & 0 & 0 \\ 0 & 0.1185 & 0 & 0 & 0 & 0 \\ 0 & 0 & 0 & 0 & 0 & 0 \\ 0 & 0 & 0 & 0 & 0 & 0 \\ 0 & 0 & 0 & 0 & 0 & 0 \\ 0 & 0 & 0 & 0 & 0 & 0.0006 \end{bmatrix}.$$

With this matrix, the compliance sum is 0.2376. Thus, after optimization, the compliance sum has improved.

4.3. Global condition index of the mechanism

One of the disadvantages for the parallel mechanisms involves the fact that they normally contain a smaller workspace. As a result, many scholars have attempted to maximize the workspace; however, one author found that the process of maximizing the workspace of parallel mechanisms could sometimes decrease the kinematic performance of the device. Subsequently, another researcher proposed the global condition index[11] for workspace optimization in order to achieve a "well-conditioned workspace". In this case, the index represents an objective function for workspace optimization. The derivation process for the index contains four steps. In the first stage, many points n_{total} are randomly selected in the possible workspace, while the second step entails verifying the location of each point inside of the workspace. This second phase is accomplished by solving inverse kinematics for each actuated input to determine if the prismatic joint falls in the range of guide ways. Thirdly, one must determine the kinematics condition index, KCI, which comprises the reciprocal of the condition number in the Jacobian matrix for every point that falls in the workspace; finally, the global condition index, η, can be obtained by multiplying KCI with the possible workspace volume (pwv) and then dividing this factor by the total number of previously selected points n_{total}:

$$\eta = pwv \cdot KCI / n_{\text{total}} \tag{27}$$

Based on this equation, the objective function for workspace optimization is η. The value of the number indicates the relative efficiency of the workspace in the mechanism. Using a similar method, such as GA, DE or PSO, the single-optimization of the global condition index for a maximum well-conditioned workspace involves the utilization of multi-objective optimization for the stiffness and workspace, as these two variables normally conflict with each other.

https://doi.org/10.1017/S0263574714002835 Published online by Cambridge University Press

5. Multi-Objective Optimization

5.1. Establishment of objective functions

Normally, an increase in the stiffness of the parallel manipulator will decrease the workspace of the parallel manipulator, while a larger workspace will reduce the stiffness of the device. As a result, designers need to find a compromise between these two variables in order to find an optimal solution according to their specific design requirements and preferences.

1. Objective functions:
   The objective functions for the compliance/stiffness and workspace are described with following equations. First, the objective function for stiffness can be written as the sum of the leading diagonal elements of the compliance matrix, such as global compliance

$$ObjF1 = \sum_{i=1}^{6} C_c(i, i). \tag{28}$$

   Since lower compliance indicates greater stiffness, the global compliance should be minimized. Alternatively, one can use the sum of the mean value and the standard deviation of the leading diagonal elements in the compliance matrix as an objective function. The mean value can represent the average compliance over the workspace, while the standard deviation indicates the compliance fluctuation. In general, lower mean values represent less deformation, whereas lower standard deviations indicate a more uniform distribution of compliance over the workspace.[12]

   The objective function for workspace is the global condition index

$$\eta = \frac{\pi \cdot R_P^2 \cdot (h_{\max} - h_{\min}) \cdot KCI}{n_{\text{total}}}. \tag{29}$$

2. Design variables:

$$D = [R_P, R_b, L, angle1, angle2].$$

3. Constraints:

$$R_P \in [0.04, 0.15]m,\ R_b \in [0.4, 0.6]m,\ \mathrm{l}_i \in [0.35, 0.5]m,\ angle1 \in [15^\circ, 45^\circ],$$
$$angle2 \in [15^\circ, 45^\circ].$$

5.2. Optimization process

The gamultiobj solver in Matlab was used to solve the problem. The following parameters were input into the system: a population size of 75; a maximum generation number of 100; the tournament selection strategy; a tournament size of 2; an intermediate crossover type; a crossover ratio of 1; a constraint-dependent mutation function; and a Pareto front population fraction of 0.35.

After optimization, the Pareto front of compliance and workspace was obtained, as illustrated in Fig. 7. This graph demonstrates a conflict between the compliance sum and the global condition index, indicating that the requirement for higher stiffness will involve a sacrifice in workspace, thus suggesting that the results are compromised. Additionally, the results lack a single optimum value; thus, the optimal solution consists of several solutions, which are known as non-dominated solutions. Since different requirements may involve the selection of different values, this graph enables designers to select from those results based on their requirements. For instance, researchers that desire higher

https://doi.org/10.1017/S0263574714002835 Published online by Cambridge University Press

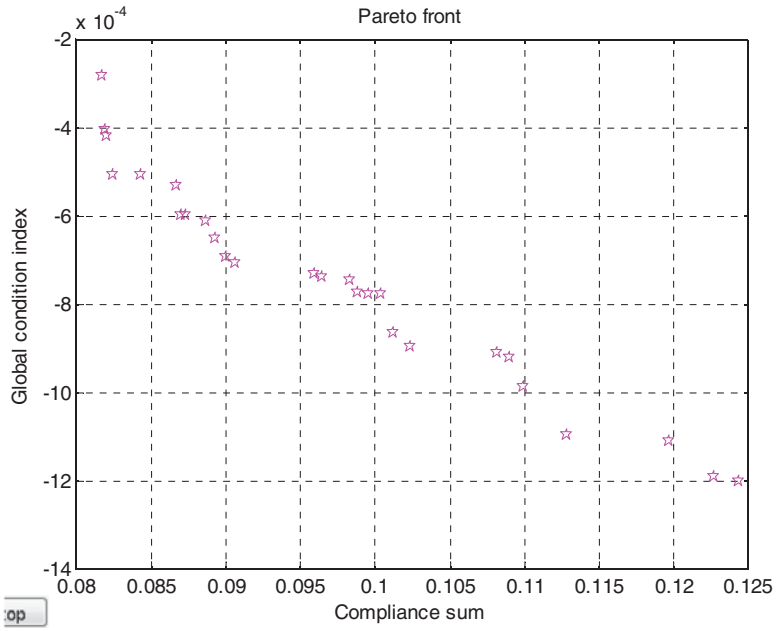


Fig. 7. Pareto front of compliance and workspace.

Table II. Typical results for objective functions and the corresponding design variables.

R_P	R_b	L	$angle1$	$angle2$	Compliance sum	Global condition index
0.1491	0.4153	0.3547	0.3721	0.3735	0.0843	−0.0005
0.1489	0.4174	0.3881	0.3997	0.3656	0.1012	−0.0008
0.1498	0.4162	0.3619	0.3795	0.3733	0.0870	−0.0005
0.1486	0.4192	0.4265	0.4237	0.3746	0.1227	−0.0012

stiffness levels may have to compromise on the workspace. Table II provides four typical results for the objective function and the corresponding design variables.

5.3. Results analysis

After optimization, the following values were selected: $R_P = 0.1491$, $R_b = 0.4153$, $L = 0.3547$, $angle1 = 0.3721$, $angle2 = 0.3735$. Based on these choices, the compliance matrix is as follows:

$$C = \begin{bmatrix} 0.0419 & 0 & 0 & 0 & 0 & 0 \\ 0 & 0.0419 & 0 & 0 & 0 & 0 \\ 0 & 0 & 0 & 0 & 0 & 0 \\ 0 & 0 & 0 & 0 & 0 & 0 \\ 0 & 0 & 0 & 0 & 0 & 0 \\ 0 & 0 & 0 & 0 & 0 & 0.0005 \end{bmatrix}.$$

In this matrix, the compliance sum is 0.0843.

https://doi.org/10.1017/S0263574714002835 Published online by Cambridge University Press

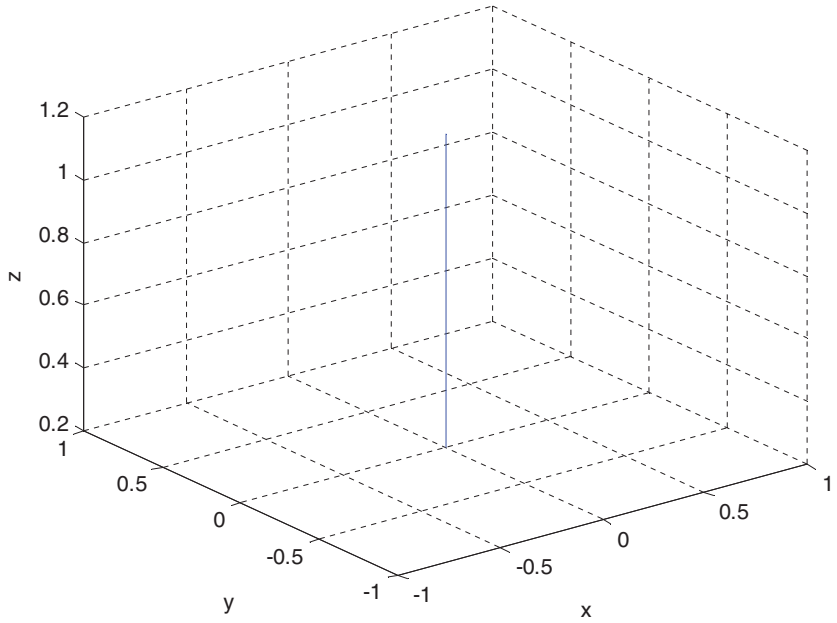


Fig. 8. Path of the moving platform center.

Before optimization, the following values were used: $R_P = 0.06$, $R_b = 0.5$, $L = 0.4$, $angle1 = 30^\circ$, $angle2 = 30^\circ$. As a result, the compliance matrix is as follows:

$$C = \begin{bmatrix} 0.3292 & 0 & 0 & 0 & 0 & 0 \\ 0 & 0.3292 & 0 & 0 & 0 & 0 \\ 0 & 0 & 0 & 0 & 0 & 0 \\ 0 & 0 & 0 & 0 & 0 & 0 \\ 0 & 0 & 0 & 0 & 0 & 0 \\ 0 & 0 & 0 & 0 & 0 & 0.0006 \end{bmatrix}.$$

The compliance sum is 0.6590, showing that after optimization, the compliance is decreased and the stiffness has increased.

After optimization, the path generated by attachment point P_1 on the moving platform is shown in Fig. 9. This research work plotted this path rather than the workspace; while workspace generally constitutes the region to which the center of the moving platform can reach, this parallel manipulator has two rotations about the X and Y axes and one translation along the Z-axis. Furthermore, due to the fact that the universal joint on the middle passive leg is attached to the center of the moving platform, this center is actually a straight line, as shown in Fig. 8.

Figure 10 shows the path that the attachment point P_1 on the moving platform generated before optimization.

In Fig. 11, the green path represents the result after optimization, while the red one represents the result before optimization. The comparison indicates that point P_1 on the moving platform can reach larger distances after optimization.

6. Dynamics of the Mechanism

In this section, the dynamics of the 3PU*S-PU hybrid manipulator are analyzed by utilizing the Lagrangian method, the results of which will be used as a guideline for controlling the manipulator. In this manipulator, u_1, u_2, and u_3 comprise the actuated joints. The Lagrangian equations can be

https://doi.org/10.1017/S0263574714002835 Published online by Cambridge University Press

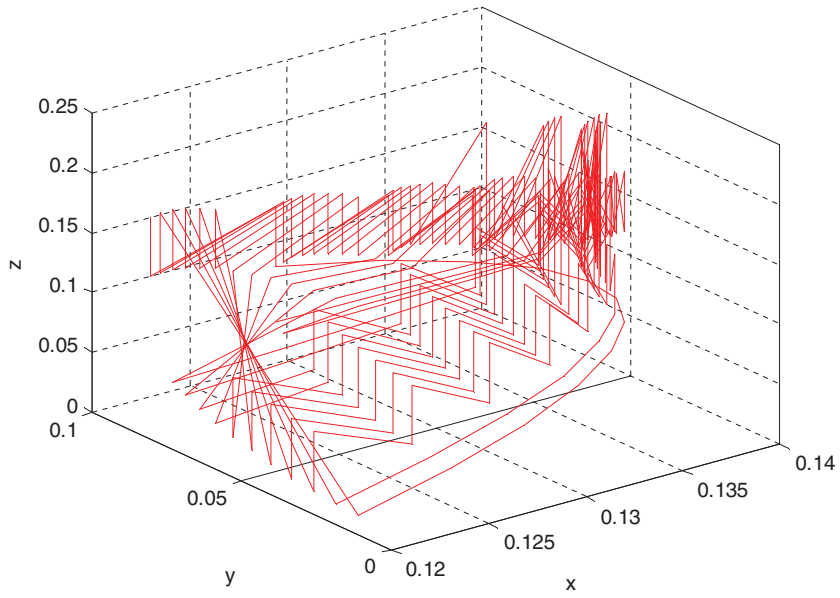


Fig. 9. Path of point P_1 after optimization.

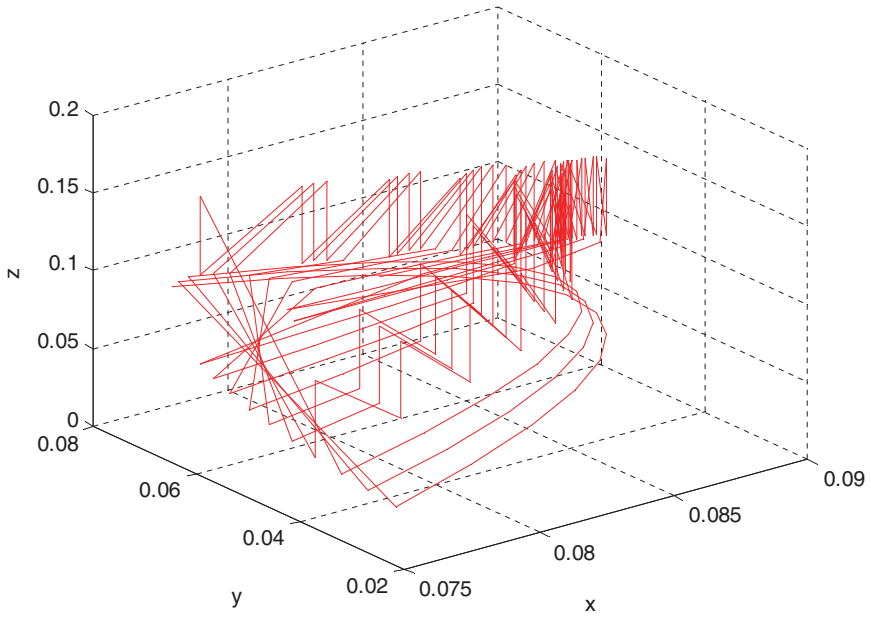


Fig. 10. Path of point P_1 before optimization.

written as follows[13]:

$$\frac{d}{dt}\left(\frac{\partial L}{\partial \dot{q}_j}\right) - \frac{\partial L}{\partial q_j} = Q_j + \sum_{i=1}^{3} \lambda_i \frac{\partial \Delta_i}{\partial q_j}, \tag{30}$$

where λ_i represents the Lagrangian multiplier and Δ_i denotes the ith constraint function. Normally, the Lagrangian equations are arranged into two sets; the first set contains the Lagrange multiplier and the second set contains the actuator forces. Given this arrangement, the first set of equations can be

https://doi.org/10.1017/S0263574714002835 Published online by Cambridge University Press

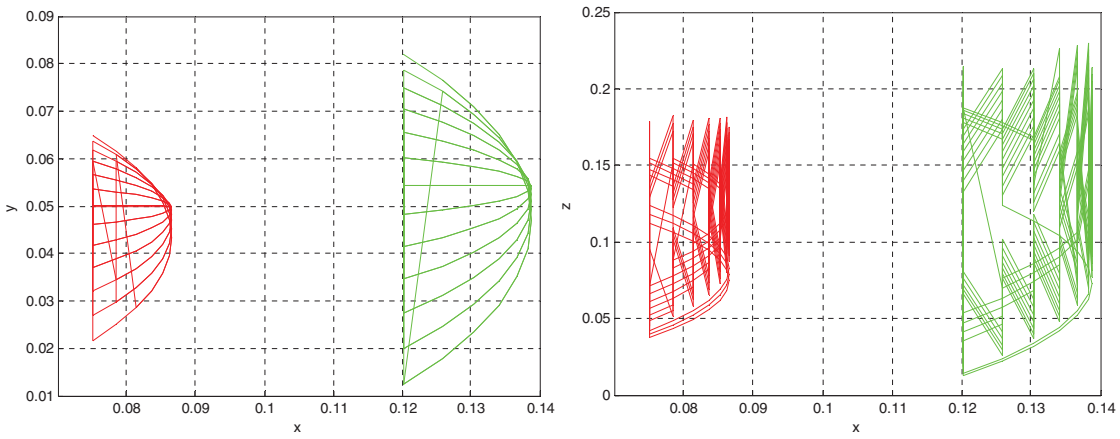


Fig. 11. Path comparison of point P_1 before and after optimization.

written as

$$\sum_{i=1}^{3} \lambda_i \frac{\partial \Delta_i}{\partial q_j} = \frac{d}{dt}\left(\frac{\partial L}{\partial \dot{q}_j}\right) - \frac{\partial L}{\partial q_j} - F_j, \tag{31}$$

where F_j is the external applied force. By inserting θ_x, θ_y, and z_e, into Eq. (31), one can obtain three equations, which can be solved for three corresponding Lagrangian multipliers. Once the multipliers are determined, the actuator forces can be solved from the second set of equations, which are provided as follows:

$$Q_j = \frac{d}{dt}\left(\frac{\partial L}{\partial \dot{q}_j}\right) - \frac{\partial L}{\partial q_j} - \sum_{i=1}^{3} \lambda_i \frac{\partial \Delta_i}{\partial q_j}, \tag{32}$$

where Q_j is the actuator force. The constraint equations can be obtained as follows:

$$\begin{aligned}\Delta_i &= |D_i E_i|^2 - \mathrm{l}_i^2 \\ &= (-R_p \cos\theta_i \sin\theta_y - R_b \cos\alpha_i + \mathrm{u}_i \cos\alpha_i)^2 + (R_p \sin\theta_i \sin\theta_x - R_p \cos\theta_i \cos\theta_x \cos\theta_y \\ &\quad - R_b \sin\alpha_i + \mathrm{u}_i \sin\alpha_i)^2 + (z_e + R_p \cos\theta_x \sin\theta_i + R_p \cos\theta_i \cos\theta_y \sin\theta_x)^2 - \mathrm{l}_i^2 \\ &= 0. \end{aligned} \tag{33}$$

The total kinetic energy of the parallel manipulator is

$$K = K_p + \sum_{i=1}^{3} K_{bi} + K_a, \tag{34}$$

where K_p is the kinetic energy of the moving platform, K_{bi} denotes the kinetic energy of the U* link of the limb, while i and K_a represent the kinetic energy of the middle passive limb.

$$K_p = \frac{1}{2} m_p \dot{z}_e^2; \quad K_{bi} = \frac{1}{2} m_b \dot{z}_e^2 + \frac{1}{2} m_b \dot{u}_i^2; \quad K_a = \frac{1}{2} m_a \dot{z}_e^2.$$

In the above equation, m_p is the mass of the moving platform, m_b is the mass of the U* link, and m_a is the mass of the middle passive limb. The total potential energy of the parallel manipulator can

https://doi.org/10.1017/S0263574714002835 Published online by Cambridge University Press

be calculated in the following equation:

$$U = U_p + \sum_{i=1}^{3} U_{bi} + U_a, \tag{35}$$

where U_p is the potential energy of the moving platform, U_{bi} denotes the potential energy of the U* link of the ith limb, and U_a signifies the potential energy of the middle passive leg.

$$U_p = m_p \cdot g \cdot z_e;\ \ U_{bi} = m_b \cdot g \cdot (z_e + R_p \cos\theta_x \sin\theta_i + R_p \cos\theta_i \cos\theta_y \sin\theta_x);\ \ U_a = m_a \cdot g \cdot \frac{z_e}{2}.$$

The Lagrangian function L can be obtained as follows:

$$L = \frac{1}{2}m_p \dot{z}_e^2 + \frac{3}{2}m_b \dot{z}_e^2 + \frac{1}{2}m_b(\dot{u}_1^2 + \dot{u}_2^2 + \dot{u}_3^2) + \frac{3}{2}m_a \dot{z}_e^2 - m_p g z_e - 3m_b g z_e - m_b g R_p \cos\theta_x(\sin\theta_1 + \sin\theta_2 + \sin\theta_3) - m_b g R_p \cos\theta_y \sin\theta_x(\cos\theta_1 + \cos\theta_2 + \cos\theta_3) - 3m_a \cdot g \cdot \frac{z_e}{2}. \tag{36}$$

By using the derivatives of the Lagrangian function with respect to the six generalized coordinates, θ_x, θ_y, z_e, u_1, u_2, and u_3, the following calculations occur:

$$\frac{\partial L}{\partial \theta_x} = m_b g R_p \sin\theta_x(\sin\theta_1 + \sin\theta_2 + \sin\theta_3) - m_b g R_p \cos\theta_y \cos\theta_x(\cos\theta_1 + \cos\theta_2 + \cos\theta_3);$$

$$\frac{d}{dt}\left(\frac{\partial L}{\partial \dot{\theta}_x}\right) = 0;$$

$$\frac{\partial L}{\partial \theta_y} = m_b g R_p \sin\theta_y \sin\theta_x(\cos\theta_1 + \cos\theta_2 + \cos\theta_3);\quad \frac{d}{dt}\left(\frac{\partial L}{\partial \dot{\theta}_y}\right) = 0;$$

$$\frac{\partial L}{\partial z_e} = -m_p g - 3m_b g - \frac{3}{2}m_a g;\quad \frac{d}{dt}\left(\frac{\partial L}{\partial \dot{z}_e}\right) = m_p \ddot{z}_e + 3m_b \ddot{z}_e + 3m_a \ddot{z}_e;\quad \frac{\partial L}{\partial u_1} = 0;$$

$$\frac{d}{dt}\left(\frac{\partial L}{\partial \dot{u}_1}\right) = m_b \ddot{u}_1;\quad \frac{\partial L}{\partial u_2} = 0;\quad \frac{d}{dt}\left(\frac{\partial L}{\partial \dot{u}_2}\right) = m_b \ddot{u}_2;\quad \frac{\partial L}{\partial u_3} = 0;\quad \frac{d}{dt}\left(\frac{\partial L}{\partial \dot{u}_3}\right) = m_b \ddot{u}_3.$$

By taking the partial derivatives of Δ_i with respect to θ_x, θ_y, z_e, u_1, u_2, and u_3, the following equations are yielded:

$$\frac{\partial \Delta_i}{\partial \theta_x} = 2(R_p \sin\theta_i \sin\theta_x - R_p \cos\theta_i \cos\theta_x \cos\theta_y - R_b \sin\alpha_i + \mathrm{u}_i \sin\alpha_i)(R_p \sin\theta_i \cos\theta_x + R_p \cos\theta_i \sin\theta_x \cos\theta_y) + 2(z_e + R_p \cos\theta_x \sin\theta_i + R_p \cos\theta_i \cos\theta_y \sin\theta_x)(-R_p \sin\theta_x \sin\theta_i + R_p \cos\theta_i \cos\theta_y \cos\theta_x)$$

$$\frac{\partial \Delta_i}{\partial \theta_y} = 2(-R_p \cos\theta_i \sin\theta_y - R_b \cos\alpha_i + \mathrm{u}_i \cos\alpha_i)(-R_p \cos\theta_i \cos\theta_y) + 2(R_p \sin\theta_i \sin\theta_x - R_p \cos\theta_i \cos\theta_x \cos\theta_y - R_b \sin\alpha_i + \mathrm{u}_i \sin\alpha_i)(R_p \cos\theta_i \cos\theta_x \sin\theta_y) + 2(z_e + R_p \cos\theta_x \sin\theta_i + R_p \cos\theta_i \cos\theta_y \sin\theta_x)(-R_p \cos\theta_i \sin\theta_y \sin\theta_x)$$

$$\frac{\partial \Delta_i}{\partial z_e} = 2(z_e + R_p \cos\theta_x \sin\theta_i + R_p \cos\theta_i \cos\theta_y \sin\theta_x)$$

$$\frac{\partial \Delta_1}{\partial u_1} = 2(-R_p \cos\theta_1 \sin\theta_y - R_b \cos\alpha_1 + \mathrm{u}_1 \cos\alpha_1)(\cos\alpha_1) + 2(R_p \sin\theta_1 \sin\theta_x$$

https://doi.org/10.1017/S0263574714002835 Published online by Cambridge University Press

$$- R_p \cos\theta_1 \cos\theta_x \cos\theta_y - R_b \sin\alpha_1 + \mathrm{u}_1 \sin\alpha_1) \sin\alpha_1$$

$$\frac{\partial \Delta_i}{\partial u_1} = 0 \quad (i = 2, 3)$$

$$\frac{\partial \Delta_i}{\partial u_2} = 0 \quad (i = 1, 3)$$

$$\frac{\partial \Delta_2}{\partial u_2} = 2(-R_p \cos\theta_2 \sin\theta_y - R_b \cos\alpha_2 + \mathrm{u}_2 \cos\alpha_2)(\cos\alpha_2)$$
$$+ 2(R_p \sin\theta_2 \sin\theta_x - R_p \cos\theta_2 \cos\theta_x \cos\theta_y - R_b \sin\alpha_2 + \mathrm{u}_2 \sin\alpha_2)(\sin\alpha_2)$$

$$\frac{\partial \Delta_i}{\partial u_3} = 0 \quad (i = 1, 2)$$

$$\frac{\partial \Delta_3}{\partial u_3} = 2(-R_p \cos\theta_3 \sin\theta_y - R_b \cos\alpha_3 + \mathrm{u}_3 \cos\alpha_3)(\cos\alpha_3)$$
$$+ 2(R_p \sin\theta_3 \sin\theta_x - R_p \cos\theta_3 \cos\theta_x \cos\theta_y - R_b \sin\alpha_3 + \mathrm{u}_3 \sin\alpha_3)(\sin\alpha_3).$$

By putting the obtained derivatives into Eqs. (31) and (32), the following dynamic equations are obtained:

$$2\sum_{i=1}^{3} \lambda_i [(R_p \sin\theta_i \sin\theta_x - R_p \cos\theta_i \cos\theta_x \cos\theta_y - R_b \sin\alpha_i + \mathrm{u}_i \sin\alpha_i)(R_p \sin\theta_i \cos\theta_x$$
$$+ R_p \cos\theta_i \sin\theta_x \cos\theta_y) + (z_e + R_p \cos\theta_x \sin\theta_i + R_p \cos\theta_i \cos\theta_y \sin\theta_x)(-R_p \sin\theta_x \sin\theta_i$$
$$+ R_p \cos\theta_i \cos\theta_y \cos\theta_x)]$$
$$= -(m_b g R_p \sin\theta_x (\sin\theta_1 + \sin\theta_2 + \sin\theta_3) - m_b g R_p \cos\theta_y \cos\theta_x (\cos\theta_1 + \cos\theta_2$$
$$+ \cos\theta_3)) - f_{px}. \tag{37}$$

$$2\sum_{i=1}^{3} \lambda_i [(-R_p \cos\theta_i \sin\theta_y - R_b \cos\alpha_i + \mathrm{u}_i \cos\alpha_i)(-R_p \cos\theta_i \cos\theta_y)$$
$$+ (R_p \sin\theta_i \sin\theta_x - R_p \cos\theta_i \cos\theta_x \cos\theta_y - R_b \sin\alpha_i + \mathrm{u}_i \sin\alpha_i)(R_p \cos\theta_i \cos\theta_x \sin\theta_y)$$
$$+ (z_e + R_p \cos\theta_x \sin\theta_i + R_p \cos\theta_i \cos\theta_y \sin\theta_x)(-R_p \cos\theta_i \sin\theta_y \sin\theta_x)]$$
$$= -m_b g R_p \sin\theta_y \sin\theta_x (\cos\theta_1 + \cos\theta_2 + \cos\theta_3) - f_{py}. \tag{38}$$

$$2\sum_{i=1}^{3} \lambda_i (z_e + R_p \cos\theta_x \sin\theta_i + R_p \cos\theta_i \cos\theta_y \sin\theta_x) = m_p \ddot{z}_e + 3m_b \ddot{z}_e + 3m_a \ddot{z}_e$$
$$- \left(-m_p g - 3m_b g - \frac{3}{2} m_a g\right) - f_{pz}. \tag{39}$$

And

$$f_1 = m_b \ddot{u}_1 - 2\lambda_1(-R_p \cos\theta_1 \sin\theta_y - R_b \cos\alpha_1 + \mathrm{u}_1 \cos\alpha_1)(\cos\alpha_1)$$
$$+ 2(R_p \sin\theta_1 \sin\theta_x - R_p \cos\theta_1 \cos\theta_x \cos\theta_y - R_b \sin\alpha_1 + \mathrm{u}_1 \sin\alpha_1) \sin\alpha_1; \tag{40}$$

$$f_2 = m_b \ddot{u}_2 - 2\lambda_2(-R_p \cos\theta_2 \sin\theta_y - R_b \cos\alpha_2 + \mathrm{u}_2 \cos\alpha_2)(\cos\alpha_2)$$
$$+ 2(R_p \sin\theta_2 \sin\theta_x - R_p \cos\theta_2 \cos\theta_x \cos\theta_y - R_b \sin\alpha_2 + \mathrm{u}_2 \sin\alpha_2) \sin\alpha_2; \tag{41}$$

$$f_3 = m_b \ddot{u}_3 - 2\lambda_3(-R_p \cos\theta_3 \sin\theta_y - R_b \cos\alpha_3 + \mathrm{u}_3 \cos\alpha_3) \cos\alpha_3$$
$$+ 2(R_p \sin\theta_3 \sin\theta_x - R_p \cos\theta_3 \cos\theta_x \cos\theta_y - R_b \sin\alpha_3 + \mathrm{u}_3 \sin\alpha_3) \sin\alpha_3. \tag{42}$$

https://doi.org/10.1017/S0263574714002835 Published online by Cambridge University Press

The multipliers can be determined through Eqs. (37)–(39). Subsequently, Eqs. (40)–(42) can yield the actuator forces. These preceding equations can serve as a guideline for controlling the hybrid manipulator. Future work will focus on the nonlinear control of this new parallel manipulator based on Lagrangian dynamics.

7. Conclusion

This paper has proposed and analyzed a novel 3-DOF hybrid manipulator, 3PU*S-PU, derived from the Gf set theory. Specifically, a description of the advantages for this new type of manipulator is followed by kinematic analysis for the purpose of subsequent performance analysis. The most important kinematic performances, stiffness/compliance, and workspace, are analyzed and optimized through DE and genetic algorithms. Subsequently, the Pareto front theory serves as the framework for conducting multi-objective optimization on the compliance and workspace of the mechanism. The results show that the two kinematic performances are improved after optimization; finally, the dynamic analysis of the mechanism is conducted based on the Lagrangian method, which establishes a foundation for subsequent control of the manipulator.

This proposed Gf set based manipulator contains the novel option of changing the original passive leg to a PU type in order to attain 3-DOF. Furthermore, this work suggests the application of U* joints as three limbs to replace conventional limbs, which greatly improves the stiffness of this hybrid manipulator. Future work will focus on the nonlinear control of this new parallel manipulator based on Lagrangian dynamics.

Acknowledgements

The authors would like to thank the Natural Sciences and Engineering Research Council of Canada (NSERC) and the Canada Research Chairs Program for their financial support towards this study.

References

1. X. J. Liu, J. S. Wang and G. Pritschow, "A new family of spatial 3-DoF fully-parallel manipulators with high rotational capability," *Mech. Mach. Theory* **40**, 475–494 (2005).
2. L. W. Tsai, *Mechanism Design: Enumeration of Kinematic Structures According to Function* (CRC Press, Boca Raton, Florida, USA, 2001).
3. O. Salgado, O. Altuzarra, V. Petuya and A. Hernandez, "Type Synthesis of a Family of 3T1R Fully-Parallel Manipulators using a Group-Theoretic Approach," *12th IFToMM World Congress on the Theory of Machines and Mechanisms,* Besancon, France (2007) pp. 18–21.
4. J. Angeles, S. Caro, W. Khan and A. Morozov, "The kinetostatic design of an innovative schonflies motion generator," *Proc. Inst. Mech. Eng. C* **220**(C7), 935–944 (2006).
5. F. Gao, J. L. Yang and Q. D. Ge, *Gf Set Theory for the Type Synthesis of Parallel Manipulators* (Science Press, Beijing, China, 2010).
6. D. Zhang and Z. Gao, "Hybrid head mechanism of the groundhog-like mine rescue robot," *Robot. Comput.-Integr. Manuf.* **27**(2), 460–470 (2011).
7. W. J. Zhang, P. R. Ouyang and Z. H. Sun, "A Novel Hybridization Design Principle for Intelligent Mechatronics Systems," *Proceedings of International Conference on Advanced Mechatronics* (ICAM2010), Osaka, Japan (Oct. 2010) pp. 4–6.
8. X. J. Liu and J. S. Wang, "Some new parallel mechanisms containing the planar four-bar parallelogram," *Int. J. Robot. Res.* **22**(9), 717–732 (2003).
9. D. Zhang, Z. M. Bi and B. Z. Li, "Design and kinetostatic analysis of a new parallel manipulator," *Robot. Comput.-Integr. Manuf.* **25**(4–5), 782–791 (2009).
10. D. Zhang, Kinetostatic Analysis and Optimization of Parallel and Hybrid Architectures for Machine Tools *Ph.D. Thesis* (Quebec, Canada: Laval University, 2000).
11. R. Stamper, L. W. Tsai and G. Walsh, "Optimization of a Three DOF Translational Platform for Well-Conditioned Workspace," *Proceedings of the IEEE International Conference on Robotics and Automation*, Albuquerque, NM, USA (1997) pp. 3250–3255.
12. D. Zhang, "Global Stiffness Optimization of Parallel Robots using Kinetostatic Performance Indices," In: *Robot Manipulators Trends and Development*, (A. Jimenez and B. M. Al Hadithi, eds.) (InTech, 2010) pp. 125–138.
13. L. W. Tsai, *Robot Analysis: The Mechanics of Serial and Parallel Manipulators* (John Wiley & Sons, Inc., New York, NY, USA, 1999).

https://doi.org/10.1017/S0263574714002835 Published online by Cambridge University Press